THE EUROPEAN
PHYSICAL JOURNAL PLUS

Numerical design and optimization of mechanical vane-type vortex generators in a serpentine air inlet duct

Iman Maghsoudi[1], **Mostafa Mahmoodi**[1,a], **Mohamad Ali Vaziri**[2]

[1] Malek Ashtar University of Technology, Tehran, Iran
[2] Malek Ashtar University of Technology, Isfahan, Shahin Shahr, Iran

Abstract The aim of this work is to investigate the design parameters and optimize the section profile of mechanical vane-type VGs in a sample serpentine air inlet duct by a validated computational model. The design parameters are the height, length, angle of attack and axial location of vortex generators. Total pressure loss (PLC), distortion coefficients (DC(60) and $\Delta P_C/P$) and swirl parameters (SC(60) and SI) are assessed in the duct aerodynamic interface plane (AIP) by using twelve layouts of straight vane-type VGs. The geometrical sensitivity analysis of the duct with straight VGs is performed by discrete adjoint formulation. The results of sensitivity analysis indicate that the critical regions of geometry are the leading and trailing edges of VG vanes. By changing straight profile into S-shape type, new VGs are investigated in eight layouts by applying the aforementioned parameters. S-type VGs improve the flow control performance in comparison with the straight ones. The optimal design points are chosen by two different methods with the goal of minimizing the flow loss metrics. Results indicate that all of the optimal design points have the S-type profile and they achieve over 70%, 40% and 20% reductions in distortion, swirl and total pressure loss coefficients at AIP plane, respectively.

List of symbols

AIP	Aerodynamic interface plane (duct exit plane or engine inlet face)
AR	Area ratio
B	Distance between two adjacent vortex generators
BLI	Boundary layer ingesting
C	Vortex generator length
CP	Pressure coefficient
D	Duct outlet diameter
DP	Design point
$\{D\}$	Vector of design variable
DC(θ)	Distortion coefficient (descriptor) for θ sector $= \left(\frac{P_\theta - P_f}{q_f} \right)$
e	Error
e_a^{21}	Approximate relative error

[a] e-mail: mostafamahmoodi@mut.ac.ir

e_{ext}^{21}	Extrapolated relative error
$\{F\}$	Aerodynamic objective function vector
GCI	Grid convergence index
h	Height of VG
I	Turbulence intensity
k	Turbulence kinetic energy
L	Duct length
LR	Duct length ratio
LRR	Launder–Reece–Rodi
LPS	Linear pressure strain
M	Mach number
p	Order of accuracy
P_{f}	AIP total pressure
P_{θ}	Total pressure in θ sector
P/P_i	Total pressure ratio
$\Delta P_C/P$	Circumferential distortion intensity (descriptor) $= \left(\frac{\text{PAV}-\text{PAVLOW}}{\text{PAV}}\right)$
PAV	Ring average total pressure
PAVLOW	Average total pressure of low total pressure region for a ring
PFAV	Face average total pressure
PR	Pressure recovery
R	Discrete residual vector
r	Grid refinement factor
q	Dynamic pressure
Re	Reynolds number
RSM	Reynolds stress model
SAE	Society of Automotive Engineers
$SC(\theta)$	Swirl distortion parameter (descriptor) $= \frac{\max\left(\overline{U_{\theta 60}}\right)}{\overline{U_x}}$
SI	Swirl intensity parameter (descriptor)
SS	Swirl sector
SVG	Submerged vortex generator
U_{θ}	Circumferential velocity
U_x	Axial velocity
$\bar{u}$	Mean velocity
u_i'	Fluctuating velocity
VG	Vortex generator
X	Computational grid position
$\rho\overline{u_i'u_j'}$	Reynolds stress term

Subscripts

max	Maximum
min	Minimum
avg, mean	Average
a	Approximate
fine	Fine grid
ext	Extrapolated
∞	Freestream

f	Engine face
i	Infinity
in	Inlet plane
t	Turbulence
I, J, K	Unit vectors in x, y and z directions

Greek symbols

δ	Boundary layer thickness
α	Flow swirl angle
ρ	Density
φ	Variable in GCI method
β	Angle of VG relative to flow direction
θ	Circumferential angle
μ	Viscosity
Λ	Adjoint vector of Lagrangian multipliers
ε	Turbulence dissipation rate
ω	Specific dissipation rate

1 Introduction

The most common types of modern diffusers are S-shaped and serpentine ducts as well. The main flow features that have caused total pressure loss and distortion in the AIP of diffusers are the separation of turbulent boundary layer and formation of secondary flow structures inside the duct. The separation phenomenon results in reduced total pressure and increased distortion and swirl at the engine face. Total pressure distortion can be detrimental to the engine compressor operability and triggers the vibration of blades and lowers the surge margin at the characteristic chart.

Passive and active flow control methods have been extensively studied in highly compact diffusers, with the goal of improving flow loss metrics at the aerodynamic interface plane (AIP). In the passive method, the mechanical VGs are used in a row to attenuate pressure losses and flow separation; and in the active method [1], continuous or pulsed jet stream is blown into the boundary layer by jet VGs. In the field of active flow control, supersonic pulsed jet was investigated in a highly compact S-duct [2, 3].

Several previous studies had investigated the usage of passive flow control methods to reduce distortion at the AIP of the ducts with rectangular [4–6] and circular cross sections [7–11]. In rectangular cross-sectional S-ducts, a sort of trapezoidal-shaped submerged vortex generator was applied in four combinations (four locations and numbers) [5]. With the best combination of SVG reported in this research, a 27% reduction in the distortion coefficient (DC60) was possible, which was reasonably higher than a 9% reduction with tapered-fin vortex generators [4]. In another research endeavor [6], fishtail-type, submerged vortex generators were investigated in an S-shaped rectangular duct and only their positional parameter was changed during the optimization process. The results indicated that the DC(60) coefficient reduced up to 16% in the best design point.

Hybrid passive and active method was also investigated at Refs. [12–15]. By applying this method, distortion was reduced up to 35% as compared with the case without flow controls [13].

Recent investigations used the combination of RANS calculation, parametric design and optimization algorithms to find the best VG configuration in terms of AIP distortion reduction [16–24].

The optimization of an S-duct inlet was studied by employing two different reduced-order computational models based on a VG model of [9, 16, 24]. The vortex generators were independently optimized with five design parameters. Shape design parameters (the length and the height) and the angle of attack represented the geometric property of the VG, while the axial and circumferential locations reflected the positional property of the VG. Results were compared with only two performance metrics of DC(60) and PR which showed up to 79% reduction in DC(60) coefficient and no changes observed in total pressure recovery.

Experimental investigation of co-rotating passive VGs was conducted in an S-duct inlet [18]. A set of nine configurations was studied by changing the height, axial position and circumferential extent of VGs as the design parameters. Results showed that DC(60) and pressure loss reduced up to 50% and 30%, respectively, for the mean flow field.

Straight passive vortex generators were studied by numerical simulations in a semi-submerged boundary layer ingesting intake [19]. The VGs design parameters were their height, angle of attack, the number of VGs, side spacing of VGs and longitudinal location of VG row. The DC(60) coefficient was reduced by a maximum of 80% over the baseline case, and only 0.35% reduction in total pressure recovery was observed at the finest design point.

Topological derivation or sensitivity was used for finding the best location of installation for a single vortex generator inside a curved air inlet duct [22, 23]. The design criterion was set for minimizing the swirl function, which was reduced by 7% in the best location of the VGs.

Flow control was experimentally conducted in an S-shaped diffuser (AR = 1.4, H/D_{in} = 1.34, which was previously investigated in Ref. [25]) by using mechanical VGs and pulsed microjets [26]. The inlet Mach number was 0.2–0.4 (Re = 1.5×10^6 based on AIP diameter). It was observed that passive VGs had better optimization than pulsed and steady jet VGs. Results showed 56% and 33% reductions in DC(60) coefficient and total pressure peak fluctuations, respectively.

Boundary layer fences and VGs were studied in an S-shaped duct in a hybrid wing body configuration [27]. Inlet velocity was 22 m/s. Upper duct surface fences caused a 11% reduction in distortion, while the pressure loss was increased by a maximum of 52%.

Numerical and experimental investigation of the submerged VGs (SVGs) was conducted in a rectangular S-duct inlet in different combinations [28]. Results showed a 27.26% increase in static pressure recovery and 14.58% decrease in total pressure loss coefficient. SVG row also caused considerable decreases (∼ 27% and ∼ 24.58%) in distortion coefficient and non-uniformity index, respectively.

The following results could be obtained according to the survey presented in the preceding paragraphs about the effect of mechanical vane-type VGs on flow improvement at the curved ducts.

Among the design parameters of VGs, the shape parameters of VG length and height, the installation parameter of the VG angle of attack and positional parameters of axial and circumferential locations have been studied and optimized. Most of these research programs were carried out on the rectangular straight profile VGs, and no effort was made to optimize their section profile.

Regarding the flow loss metrics in the duct exit plane, only DC(60) distortion coefficient, $\Delta P_C/P$ circumferential distortion coefficient and pressure recovery (PR) were studied, and other prominent metrics such as SI and SC(60) flow swirl parameters were not taken into consideration as a figure of merit of the flow improvement in AIP of the ducts.
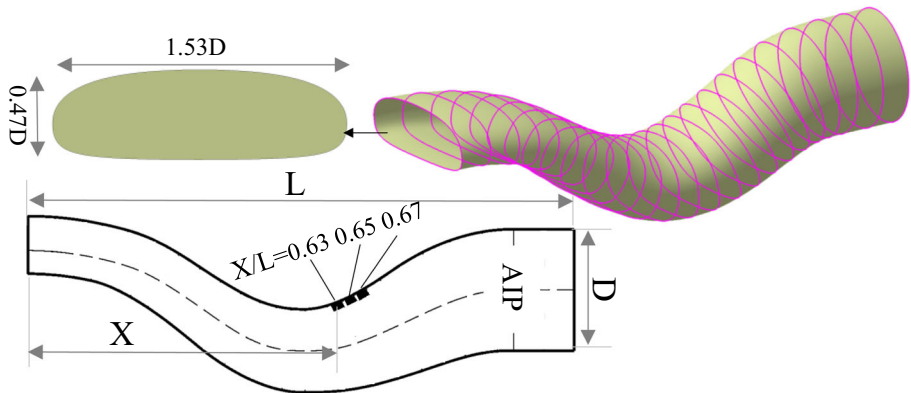
Fig. 1 Serpentine duct geometry and VG rows longitudinal locations

As regards the choice of the best design points of VGs, the efficacy of all flow loss metrics has not been aggregately considered so far.

In addition to optimizing the design parameters of shape, installation and the position of VGs, the present work also addresses their section profile optimization with the help of the sensitivity analysis by the adjoint solver in a sample serpentine duct. The flow loss metrics of DC(60) and $\Delta P_C/P$ (distortion metrics), SI and SC(60) (flow swirl parameters) and PLC (total pressure loss) would be assessed and compared in each design point. The optimal design points (DPs) would be eventually chosen by two methods with the goal of minimizing loss at AIP for the future experimental research.

2 Serpentine duct and flow control characteristics

2.1 Serpentine duct

The duct that is investigated in this paper is a double-S-shape (serpentine) full-scale diffuser (Fig. 1). The ratios of length-to-diameter (L/D_{AIP}) and outlet-to-inlet diffusion area (AR = A_{exit}/A_{inlet}) of the duct are 4.2 and 1.3, respectively. Duct AIP is considered to be $0.15L$ upstream of engine face.

2.2 Vane-type VGs design parameters

Effective design parameters of mechanical vane-type VGs are shown in Fig. 2 and tabulated in Table 1 for the straight- and S-type VGs.

VG row installation pattern is selected as co-rotating based on the results of Refs. [26, 29, 30] (Fig. 2). The main advantage of the co-rotating pattern of VGs is their downstream effectiveness, resulting in a more effective use of the vortex energy within the boundary layer.

In order to reduce unknown parameters in this research, the three factors of number, row installation angle (the angle of VG row relative to the flow direction) and VGs lateral spacing are preferred to be fixed (Table 2).

In order to assess the approximate installation region of the VGs, a VG row was initially studied in five different axial locations ($X/L = 0.61, 0.63, 0.65, 0.67$ and 0.69) on the
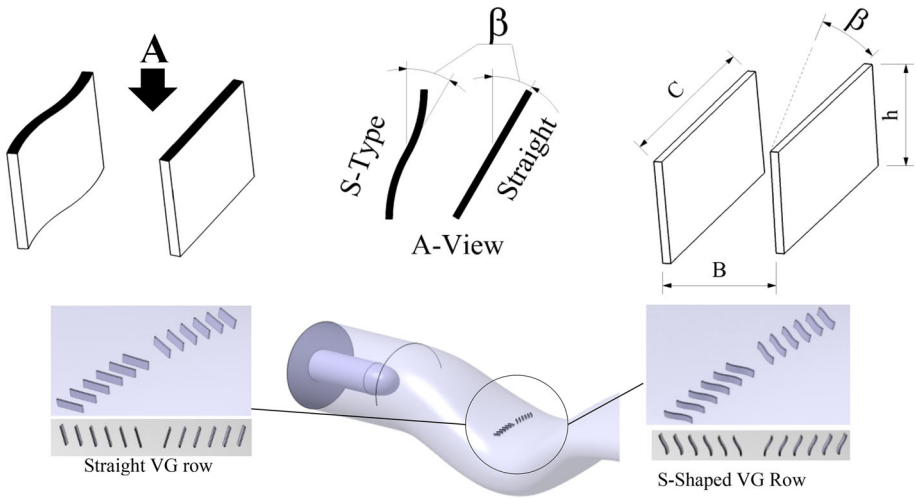
Fig. 2 Design parameters and installation pattern of straight- and S-type VGs

Table 1 Design parameters of straight- and S-type VGs

Design parameters	Symbol	VG type		Value
		Straight-type	S-type	
VG row installation location	*X/L*	✓	✓	0.63
		✓	✓	0.65
		✓	✓	0.67
Vane length	*C/L*	✓	✓	0.016
		✓	✓	0.025
		✓	✓	0.025
Vane height	*h/D*	✓	✓	0.042
		✗	✓	15
VGs angle of attack	*β*	✓	✓	22.5
		✓	✓	30

Table 2 Design fixed parameters of VGs

Design fixed parameters	
Number of VGs	12 (6 on each side)
VG row installation angle (°)	90
VGs lateral spacing (*B/D*)	0.0416

upper surface of the duct aft bend and three locations were selected for subsequent analysis accordingly (Fig. 1).

Fig. 3 Loss 60° sector for calculating DC(60) distortion coefficient
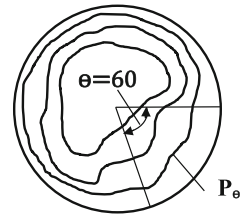
3 Duct flow loss metrics

Several metrics have been proposed to quantify flow loss at the duct AIP. The aerodynamic behavior of the flow in the duct outlet is quantified by the total pressure loss. The stability pressure ratio is assessed by distortion descriptors, and the severity of cross-flow velocities is determined by swirl descriptors. These metrics are defined as follows.

3.1 Total pressure loss coefficient

Duct total pressure loss coefficient is defined as the difference between the ambient and the duct exit average total pressures, normalized by the freestream total pressure [31]:

$$\text{Pressure loss coefficient (PLC)} = \frac{P_\infty - P_\text{f}}{P_\infty} \tag{1}$$

3.2 Distortion descriptor first definition (DC(θ))

In this approach, the distortion coefficient is defined as the difference between the engine face or AIP average total pressure (P_f) and the lowest average total pressure in any sector defined by a critical angle of θ (P_θ) at the exit plane, normalized by the dynamic pressure at the duct exit [31]:

$$\text{DC}(\theta) = \left(\frac{P_\theta - P_\text{f}}{q_\text{f}} \right) \tag{2}$$

In most cases, theta angle is considered to be 60°. In Fig. 3, the maximum total pressure loss sector for calculating the DC(60) coefficient is shown.

3.3 Distortion descriptor second definition ($\Delta P_\text{C}/P$)

This definition is known as the circumferential distortion coefficient, which is expressed by the $\Delta P_\text{C}/P$ factor [32, 33].

$\Delta P_\text{C}/P$ coefficient depends upon the number and size of pressure deficit regions in AIP. This type of measurement is executed by the standard total pressure rake with five rings (Fig. 4). The average total pressure of the maximum loss region of the ring and circumferential distortion intensity is calculated as follows [32, 33]:

$$\text{Circumferential intensity:} \left(\frac{\Delta P_\text{C}}{P} \right)_i = \left(\frac{\text{PAV} - \text{PAVLOW}}{\text{PAV}} \right) \tag{3}$$
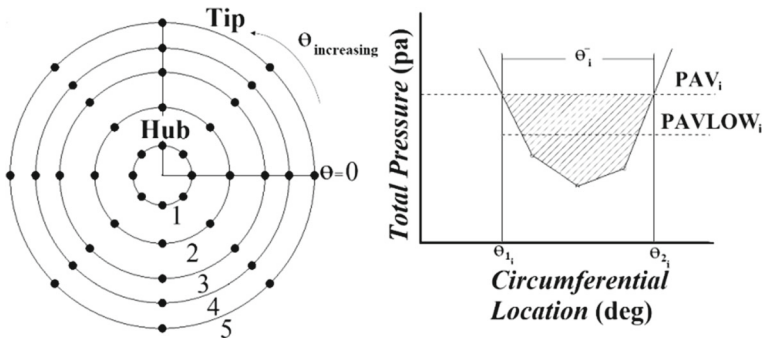
Fig. 4 AIP 40 pressure transducer locations in five rings and $\Delta P_C/P$ calculation graph at the ith ring

3.4 Swirl descriptor first definition (SC(θ))

The first descriptor that is counterparts for the DC(60) distortion coefficient is the SC(60) swirl coefficient [31, 34]. This factor assesses the severity of cross-flow velocities at the AIP and is calculated as follows:

$$SC(60) = \frac{\max(\overline{U_{\theta 60}})}{\bar{U}_x} \tag{4}$$

where $U_{\theta 60}$ is the maximum AIP circumferential velocity over a 60° sector and U_x is the mean axial velocity at AIP.

3.5 Swirl descriptor second definition (SI)

SAE [35] proposed the second approach for swirl estimation that is defined as swirl intensity (SI), used to quantify swirl distortion. In this approach, the AIP is divided into several radial rings (analogous to the rings in Fig. 4 for circumferential distortion descriptor), and the descriptors are calculated at each radial position based on the ring swirl angle distribution for each snapshot. The swirl angle is specified as the circumferential angle of flow from the axial direction of the velocity vector. Positive swirl angle is in the direction of the fan or compressor rotation.

$$\alpha = \tan^{-1}\left(\frac{U_\theta}{U_x}\right) \tag{5}$$

The swirl angle distribution is divided into positive and negative angle regions, and the swirl sector elements are defined as:

$$SS_{i,k}^+ = \frac{1}{\theta_{i,k}^+} \int_{\theta_{i,k}^+} \alpha(\theta)_{i,k}\,d\theta \tag{6}$$

$$SS_{i,k}^- = \frac{1}{\theta_{i,k}^-} \int_{\theta_{i,k}^-} \alpha(\theta)_{i,k}\,d\theta \tag{7}$$

where $\alpha(\theta)_{i,k}$ is the swirl angle as a function of the circumferential location from the data point in the given extent. Swirl intensity is defined as the extent weighted absolute swirl for ring i:

$$\mathrm{SI}_i = \frac{\sum_{k=1}^{m} \mathrm{SS}_{i,k}^+ \times \theta_{i,k}^+ + \sum_{k=1}^{m} \left| \mathrm{SS}_{i,k}^- \right| \times \theta_{i,k}^-}{360} \tag{8}$$

where m is the total number of swirl pairs from $k = 1$ to $k = \mathrm{m}$ [34, 36]. The maximum and overall average swirl intensity SI for five rings are defined in the AIP as:

$$\max(\mathrm{SI}) = \max_{i=1\ldots5}(\mathrm{SI})_i \tag{9}$$

$$\overline{\mathrm{SI}} = \frac{1}{5} \sum_{i=1}^{5} (\mathrm{SI})_i \tag{10}$$

4 Numerical method and boundary conditions

A three-dimensional viscous CFD simulation with the ANSYS Fluent solver is used in this study to predict the flow loss metrics in a serpentine duct. The Reynolds stress model with the stress-omega formulation of the pressure strain term was selected for subsequent analysis.

4.1 Reynolds stress-transport equations

Unlike one and two turbulence equation models that use isentropic eddy viscosity assumption, RSM method solves Navier–Stokes equations through Reynolds stress-transport functions with a dissipation rate equation. This implies that further five transport equations and seven additional transport equations were required for 2D and for 3D flows, respectively, so the RSM equations account for the effects of streamline curvature, swirl, rotation and rapid changes in strain rate in a more rigorous manner than one-equation and two-equation models, so it has greater potential to give accurate predictions for complex flows. The exact transport equations may be written as Eq. (11) for the transport of the Reynolds stresses:

$$\underbrace{\frac{\partial}{\partial t}\left(\rho \overline{u_i' u_j'}\right)}_{\text{Local time derivative}} + \underbrace{\frac{\partial}{\partial t}\left(\rho u_k \overline{u_i' u_j'}\right)}_{C_{ij} = \text{Convection}}$$

$$= \underbrace{-\frac{\partial}{\partial x_k}\left[\rho \overline{u_i' u_j' u_k'} + \overline{P'\left(\delta_{kj} u_i' + \delta_{ik} u_j'\right)}\right]}_{D_{T,ij} \equiv \text{Turbulet diffusion}}$$

$$+ \underbrace{\frac{\partial}{\partial x_k}\left[\mu \frac{\partial}{\partial x_k}\left(\overline{u_i' u_j'}\right)\right]}_{D_{L,ij} = \text{Molecular diffusion}} \underbrace{-\rho\left(\overline{u_i' u_k'}\frac{\partial u_j}{\partial x_k} + \overline{u_j' u_k'}\frac{\partial u_i}{\partial x_k}\right)}_{P_{ij} = \text{Stress production}} \underbrace{-\rho\beta\left(g_i \overline{u_j' \theta} + g_j \overline{u_i' \theta}\right)}_{G_{ij} = \text{Buoyancy production}}$$

$$+ \underbrace{\overline{P'\left(\frac{\partial u_i'}{\partial x_j} + \frac{\partial u_j'}{\partial x_i}\right)}}_{\varphi_{ij} = \text{Pressure strain}} \underbrace{- 2\mu \overline{\frac{\partial u_i'}{\partial x_k}\frac{\partial u_j'}{\partial x_k}}}_{\varepsilon_{ij} = \text{Dissipation}} \underbrace{- 2\rho\Omega_k\left(\overline{u_j' u_m'}\varepsilon_{ikm} + \overline{u_i' u_m'}\varepsilon_{jkm}\right)}_{F_{ij} = \text{Production by system rotation}}$$

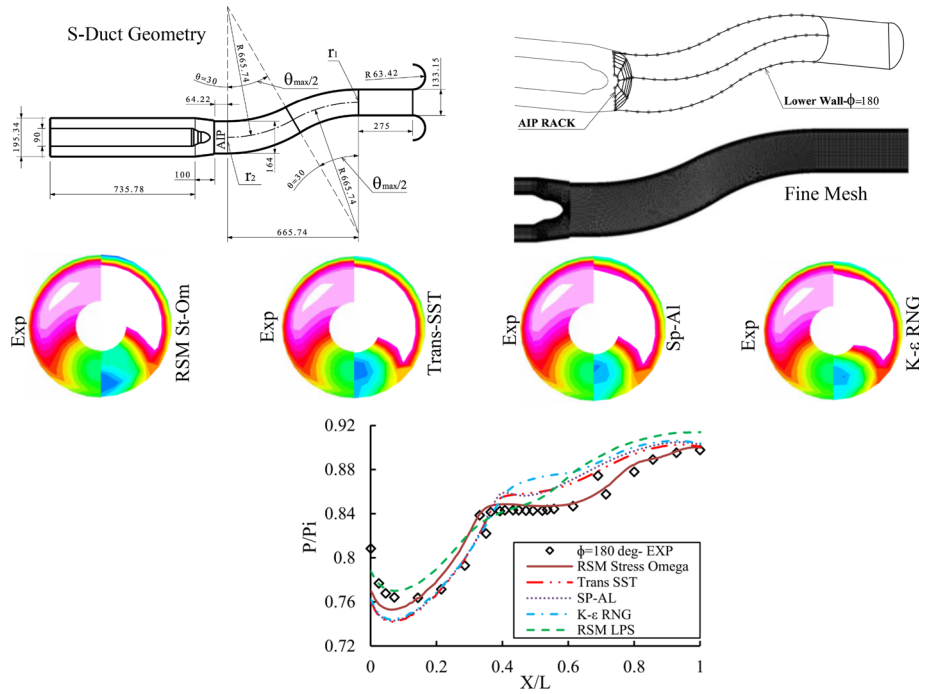$$+ \underbrace{S_{\text{user}}}_{\text{User - Defined Source Term}} \tag{11}$$

Fig. 5 Comparison of S-duct pressure contours and lower wall ($\phi = 180$) pressure coefficient at different turbulence models with experimental results ($M_{\mathrm{AIP}} = 0.4$) [47]

The main difference between the RSM equations is in the modeling of the pressure strain term in Eq. (11). The pressure strain term is modeled by two methods of ε-based and ω-based equations.

Generally, ε-based equations have weaknesses in the simulation of flow in the boundary layer and especially the flow separation phenomenon. In order to get around this problem, the Reynolds stress model that had ω-based equations as the scale-determining equation (RSM stress-omega model) was used for the present work. This model is a stress-transport model which is composed of the ω-equations and Launder–Reece–Rodi (LRR) model [37].

4.1.1 Turbulence model validation

The RSM stress-omega turbulence model for simulation of flow in the curved ducts has been extensively validated and verified through the comparison of numerical and experimental results [38–47]. In this research, an S-duct diffuser is selected for the validation of this turbulence model. This diffuser was used as a CFD validation case at the 1st and 2nd Propulsion Aerodynamic Workshop (PAW01 & PAW02), organized by AIAA Air Breathing Propulsion System Integration Technical Committee (ABPSI) (Fig. 5). The experimental test of the S-duct was carried out at $M_{\mathrm{AIP}} = 0.4$ [26].

In Fig. 5, the numerical solutions of four different turbulence models are compared with the RSM stress-omega model and experimental data [47]. Turbulence equations are Spalart–Allmaras one-equation, K–ε RNG two-equation, transition-SST four-equation and RSM-LPS seven-equation models. The grid resolution study was performed on this model based on the

Table 3 Lower wall pressure plateau error for several turbulence models [47]

Lower wall pressure plateau error (%)	
Spalart–Allmaras	1.73
RSM-LPS	1.15
Transition SST	1.7
K–ε RNG	2.67
RSM stress-omega	0.43

Table 4 Comparison of pressure recovery and distortion coefficient at AIP plane [43]

Duct type	P/P_0		$\Delta P_C/P_{avg}$	
	VG	Baseline	VG	Baseline
Experimental value	0.9761	0.97	0.0143	0.02
Spalart–Allmaras	0.9768	0.9717	0.018	0.0365
Transition SST	0.9771	0.9724	0.0181	0.0341
RSM stress-omega	0.9738	0.9699	0.0138	0.031

method, which will be presented for the serpentine duct of the present study in Sect. 4.4.1, and the fine mesh model was selected for numerical analysis.

The experimental data in Fig. 5 show the adverse pressure gradient as well as the region of separated flow indicated by a pressure plateau between $0.35 < X/L < 0.6$. This trend is well simulated by the RSM stress-omega model. After the pressure plateau zone ($X/L > 0.6$), the estimated values of the pressure coefficient are also close to the experimental results; however, in other turbulence models, onset point of pressure plateau happens at the higher pressure coefficients, the longitudinal position of separation onset is in the downstream of the experimental results, and curve slope is different in the separation region [47].

Average lower wall pressure plateau error (Table 3) reveals that the RSM stress-omega model has the minimum error (0.43%) between five studied turbulence models. This indicates that RSM St-Om model can accurately assess the adverse pressure gradient and separated flow parameters in the duct.

The results of the flow loss metrics at AIP plane show that the RSM stress-omega model most closely matches the measured recovery. In addition, the distortion values almost fall within the 95% confidence intervals for both circumferential and radial quantities [39].

In the baseline and VG S-duct (Table 4), prediction of pressure recovery by three turbulence models is almost the same [43]. However, there is a large difference in the magnitude of distortion coefficient and RSM St-Om model has the closest $\Delta P_C/P_{avg}$ values to the experimental results.

4.2 Calculation algorithm and convergence criteria

The pressure-based segregated algorithm was applied to the numerical solution, and the SIMPLE scheme was selected for pressure–velocity coupling. Spatial discretization was set as least squares cell based for gradient and the second order for pressure, density, momentum, turbulence viscosity and energy quantities. In air properties setting, the density formulation was set as an ideal gas, so the solver uses the ideal gas law for density calculation and consequently takes into account the effects of compressibility of flow during the solution.
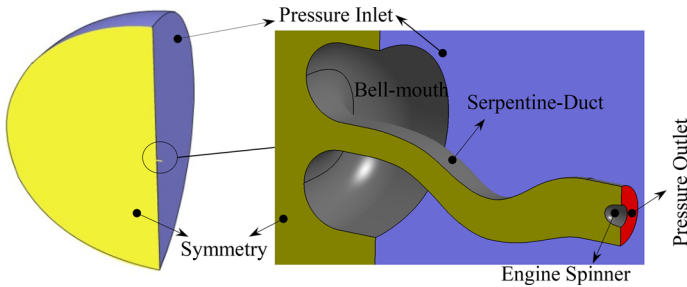
Fig. 6 Numerical domain boundary conditions

All the analysis was performed in steady-state conditions. In steady-state calculation, governing equation for the pressure-based solver does not contain time-dependent terms.

The convergence criteria of the numerical solution were set so that the residuals diagram achieved the accuracy of 0.000001 and estimated values of AIP total pressure and axial velocity achieved the accuracy of 0.000001 in the 500 final consecutive iterations.

4.3 Boundary conditions

Inlet and outlet boundary conditions were considered to be pressure inlet (at the static condition in ground) and the pressure outlet at outer space and at the end of the duct, respectively (Fig. 6). In order to provide more realistic inlet boundary condition, a bell-mouth intake is modeled in front of the duct; therefore, it makes it possible to study the effect of the inlet boundary layer in the flow field of the serpentine duct. Duct flow was analyzed for the ground static test by adjusting the pressure of AIP to achieve design mass flow rate at cruise flight condition and AIP Mach number of $M_{\mathrm{AIP}} = 0.4$.

4.4 Grid topology

Due to the symmetrical shape of the solution domain, structured fine-grid generation was performed by multiblock strategy in ANSYS ICEM software on a half model and the number of grids was set to be $\sim 8 \times 10^6$ based on the grid resolution study (see Sect. 4.4.1).

In order to have a correct solution at the viscous sublayer, the grid had layers of prism near the wall to fulfill the condition of $Y^+ < 1$ and allow appropriate resolution of the boundary layer. Elements of the internal domain of the duct and bell mouth were of the O-grid type that led to the creation of five and nine blocks inside and outside the duct, respectively (Fig. 7). Outside the duct, blocks number 1 and 2 were the inviscid O-type grid and blocks number 3, 4 and 5 were the viscous O-type grid. Inside the duct, D1 to D6 blocks were inviscid H-Type grid and V1 to V3 blocks were the viscous O-type grid. In the case of passive flow control, structured grid blocks around the vanes were increased. As shown in Fig. 7, blocks around the vanes are the viscous O-type grid.

4.4.1 Grid resolution study

A grid sensitivity study was carried out to be sure about the independence of the grid used in analyses. Three computational grids were generated to determine the optimum acceptable grid size, which had spatial resolution of coarse (0.5×10^6), medium (2.6×10^6) and fine (8×10^6) meshes (Fig. 8).

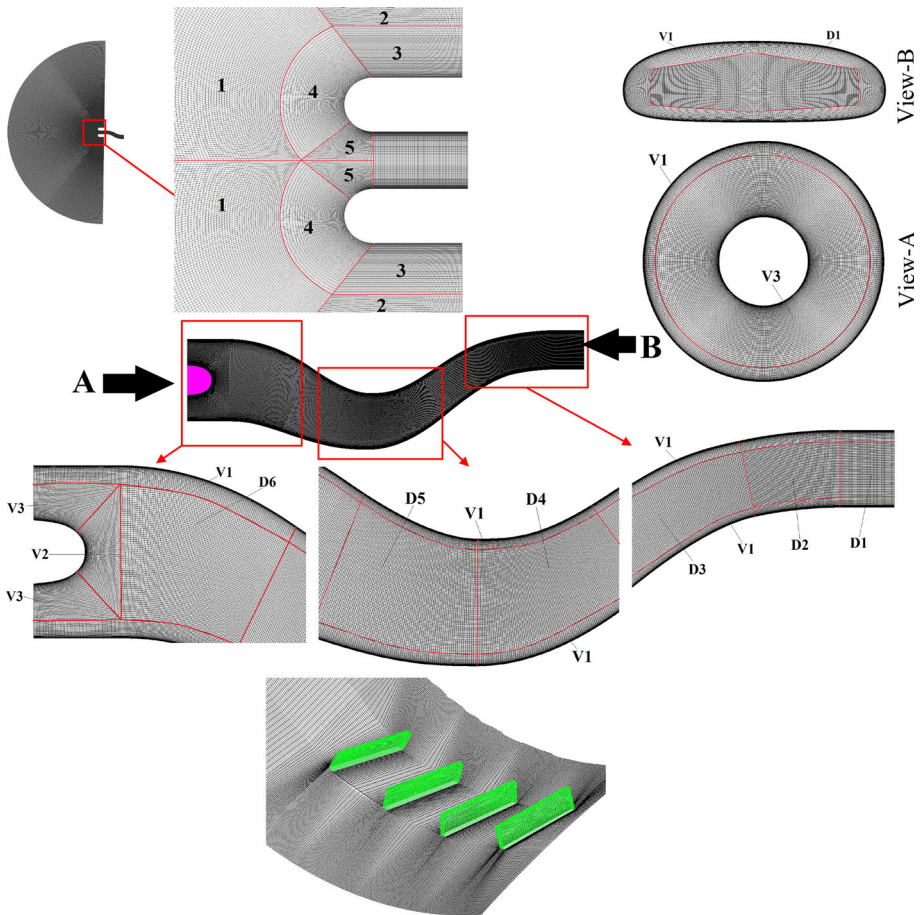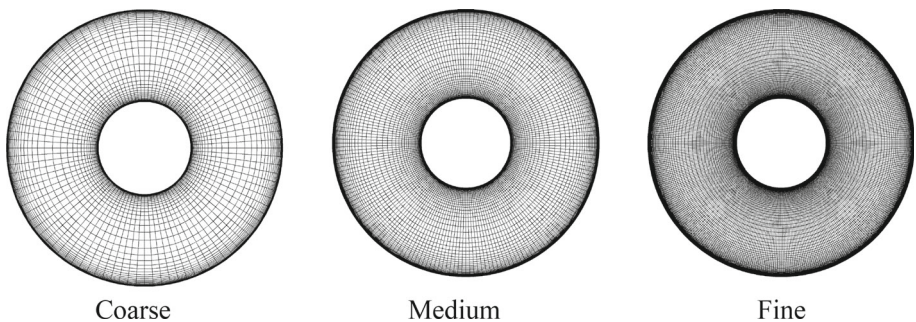**Fig. 7** Structured fine-grid blocks of serpentine baseline and mechanical VGs ducts

Fig. 8 Coarse, medium and fine mesh in the duct exit plane

Discretization error was assessed by grid convergence index method (GCI) [48]. Total pressure and axial velocity in the AIP were selected as the critical variables that were important to the objective of the simulation study. The reason behind this choice was that the

assessment of the flow loss metrics depended directly on these two parameters at the end of the duct, especially total pressure (see Sect. 3). In Table 5, r_{21} is the grid refinement factor of N1 and N2 grids, φ_{ext} is the extrapolated variable, e_a^{21} is the approximate relative error, e_{ext}^{21} is the extrapolated relative error and GCI_{fine}^{21} is the fine-grid convergence index [48].

According to Table 5, the numerical uncertainty in the fine-grid solution is 0.00127% and 0.0096% for the total pressure and axial velocity at AIP, respectively. These discretization errors are very small, giving confidence that the mesh resolution is sufficiently fine to support the conclusions of this research.

5 Results and discussion

According to the VGs design parameters in Table 1, the total of 60 design points (DPs) was selected for further analysis. The results of the analysis were assessed at the duct AIP by flow loss metrics. To facilitate the process of reviewing the results, the analysis was divided into twelve and eight layouts for straight- and S-type VGs, respectively. Each layout comprises three design points in $X/L = 0.63$(A), $X/L = 0.65$(B) and $X/L = 0.67$(C) locations in constant height, angle of attack and length of the VGs (Tables 6 and 7).

5.1 Straight VGs design points

In Figs. 9 and 10, the results of straight VGs DPs (Table 6) are compared with the baseline duct in two aspects of AIP total pressure ratio contours and upper surface pressure coefficient at $0.6 < X/L < 1$ (separation zone). It should be noted that, since the pressure data of the upper surface are the same for all DPs in the first half of the duct and upstream of the VG rows ($0 < X/L < 0.6$), the CP curve is only plotted for the second half of the duct ($0.6 < X/L < 1$).

In the baseline duct CP curve, the flow decelerates and becomes more prone to flow separation. The latter eventually occurs slightly downstream from $X/L = 0.61$. The flow separation is visible by the pressure plateau between $0.62 < X/L < 0.82$. The precise location of the separation onset is difficult to determine, although it is definitely downstream of $X/L = 0.61$. After the plateau zone, the flow is expected to re-attach briefly downstream from $X/L = 0.82$.

A large total pressure deficit region arises in the upper half of the AIP plane, which originates from the upper wall flow separation at the baseline duct. The flow streamlines at separation region reveal that a pair of strong counter-rotating vortical structures arise and extend up to the AIP plane. Two other pressure deficit regions arise in the right and left sides at the lower half of AIP, which signifies the formation of a secondary flow inside the duct bends (Fig. 9).

At all A and B DPs, VGs alter the structure of separated flow and relocate the pressure deficit region toward the circumference of the AIP (Fig. 9); however, they are unable to completely mitigate loss and separation of the duct upper surface and only the extent of the pressure deficit region is reduced (Fig. 9). It can be inferred that VGs try to restructure the secondary flow field inside the separation bubble and divide the baseline duct pressure deficit region into two weaker zones on the upper right and left sides of the AIP.

In the most C DPs, the shape and extent of the loss region do not significantly change and the pressure deficit region is more centrally located in comparison with the baseline case (ST1-C, ST2-C, ST5-C, ST7-C, ST9-C, ST11-C). This indicates that the VGs could not affect the flow, which may be attributed to the fact that they are completely located inside the separated flow region (separation bubble). Total pressure contours at ST4-C, ST6-C, ST8-

Table 5 Discretization error of critical variables at AIP

N_1, N_2, N_3	r_{21}	r_{32}	Variable (φ)	φ_1	φ_2	φ_3	p(Order of accuracy)	$\varphi_{\text{ext}}^{21}$	e_a^{21} (%)	e_{ext}^{21} (%)	GCI_{fine}^{21} (%)
$0.5 \times 10^6, 2.6 \times 10^6, 8 \times 10^6$	1.75	1.413	P/P_{o}	0.979	0.979	0.980	4.303	0.979	0.01023	0.00102	0.00127
			$U_x/\bar{U}$	0.986	0.988	0.997	5.482	0.9864	0.1561	0.0077	0.0096

Table 6 Straight VGs layouts

Layout	Straight VGs design parameters					
	C/L	β	h/D	X/L		
				A	B	C
ST1	0.016	15	0.025	0.63	0.65	0.67
ST2	0.016	15	0.042	0.63	0.65	0.67
ST3	0.016	22.5	0.025	0.63	0.65	0.67
ST4	0.016	22.5	0.042	0.63	0.65	0.67
ST5	0.016	30	0.025	0.63	0.65	0.67
ST6	0.016	30	0.042	0.63	0.65	0.67
ST7	0.025	15	0.025	0.63	0.65	0.67
ST8	0.025	15	0.042	0.63	0.65	0.67
ST9	0.025	22.5	0.025	0.63	0.65	0.67
ST10	0.025	22.5	0.042	0.63	0.65	0.67
ST11	0.025	30	0.025	0.63	0.65	0.67
ST12	0.025	30	0.042	0.63	0.65	0.67

Table 7 S-type VGs layouts

Layout	S-type VGs design parameters					
	C/L	β	h/D	X/L		
				A	B	C
SS1	0.016	22.5	0.025	0.63	0.65	0.67
SS2	0.016	22.5	0.042	0.63	0.65	0.67
SS3	0.016	30	0.025	0.63	0.65	0.67
SS4	0.016	30	0.042	0.63	0.65	0.67
SS5	0.025	22.5	0.025	0.63	0.65	0.67
SS6	0.025	22.5	0.042	0.63	0.65	0.67
SS7	0.025	30	0.025	0.63	0.65	0.67
SS8	0.025	30	0.042	0.63	0.65	0.67

C, ST10-C and ST12-C show that the higher height of the VGs could positively affect the flow, and accordingly, the separation is diminished at the upper surface of the duct. This is presumably attributed to the fact that the VGs come out of the separation bubble at these DPs and their effectiveness is increased.

By considering the CP curves of the DPs in Fig. 10, It can be deduced that, as the flow passes through the VGs, a local minimum arises at the VG row locations, which implies that the flow is accelerated via VGs. Provided that a VG row is located inside the separation bubble (in most of the C DPs), this local minimum disappears and the effectiveness of VGs is reduced.

The length of the pressure plateau region features the onset and the end of the separation bubble, and this length reduces in most A and B DPs as compared with the baseline duct (Fig. 10).
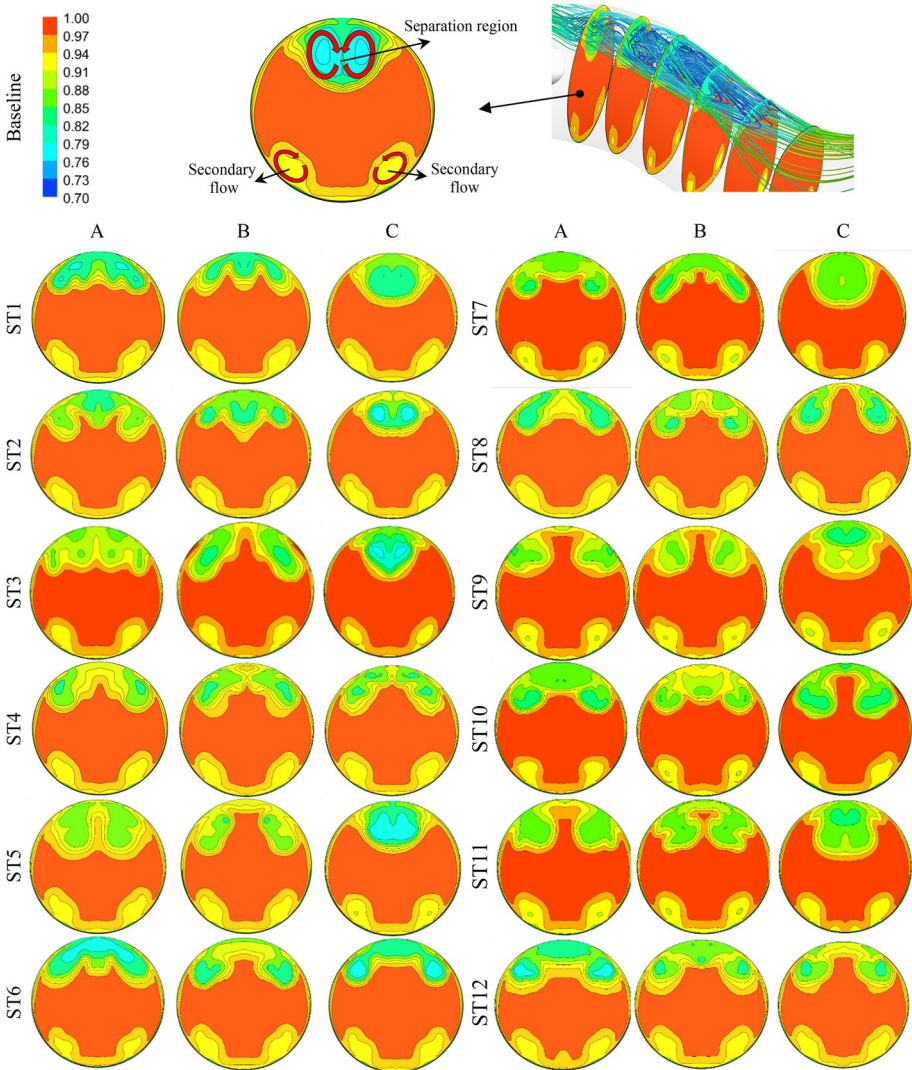
Fig. 9 AIP total pressure contours at straight VGs design points

Increasing the angle of attack at the constant VG heights of $h/D = 0.025$ and $h/D = 0.042$ causes the significant flow improvement of B DPs at ST1, ST3 and ST5 layouts and ST2, ST4 and ST6 layouts, respectively.

It can be deduced from total pressure contours that height increment of VGs at the constant angle of attack and VGs length makes them come out of the separation bubble at C DP and accordingly increase their efficacy in separation zone. Another notable point is that combining the effects of increasing the length and height of VGs provides the greatest improvement in flow recovery at C DPs.

Considering the analysis results of ST9–ST12 layouts, it can be deduced that, by combining the effects of increasing the length and angle of attack at straight profile VGs, their
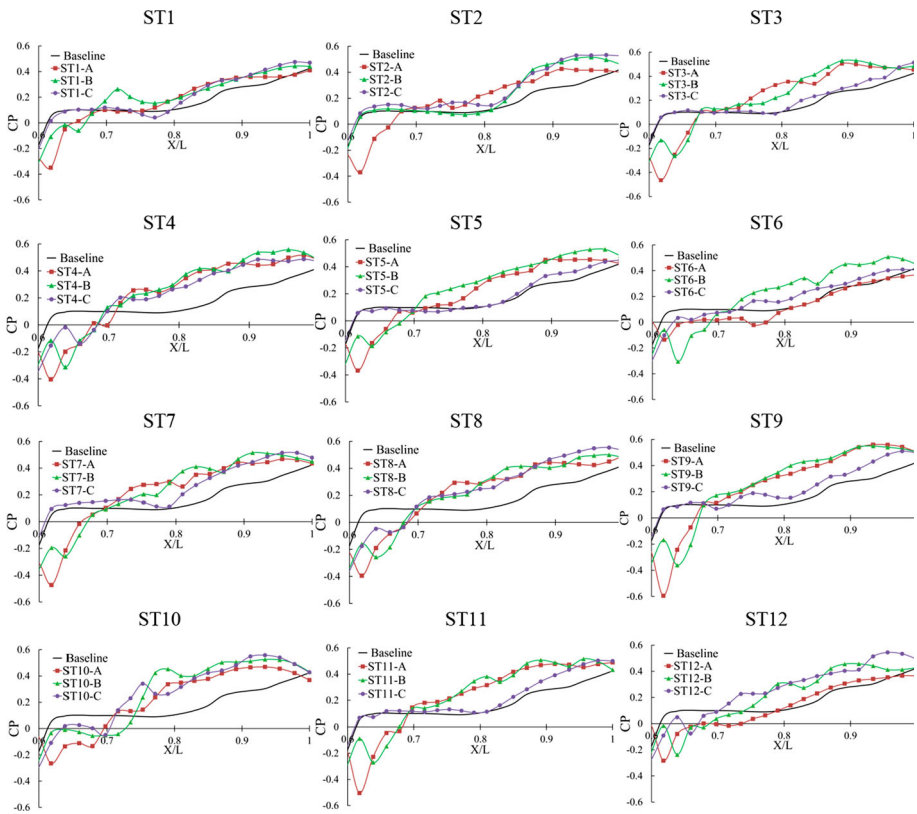
Fig. 10 Duct upper surface CP curves at straight VGs design points

effectiveness is reduced as compared with ST3–ST6 layouts. It can be inferred that the angle of attack of VGs induces a large change in the flow direction toward the side walls. Consequently, a recirculation region of flow emerges at the center of the duct upper surface just downstream of the VGs.

5.2 Optimization of passive VGs

In order to optimize the shape of the VGs and achieve higher recovery of flow in AIP, the geometrical sensitivity analysis is performed on straight VGs by discrete adjoint formulation.

5.2.1 Sensitivity analysis

The discrete residual (DR) of flow equations in steady-state form is dependent on three factors of flow variable vector (FVV), grid position in computational domain (GP) and design variable vector (DVV) (see Eq. (12)). Likewise, the performance objective function (POF) vector (or observable of interest) is also dependent on the aforementioned factors (see Eq. (13)) [49, 50]:

$$\{DR\} = \{DR(FVV, GP, DVV)\} = \{0\} \tag{12}$$

$$\{POF\} = \{POF(FVV, GP, DVV)\} \tag{13}$$

By differentiating Eqs. (12) and (13) with respect to the design variable vector (DVV), the sensitivity derivatives of the performance objective functions are calculated as follows:

$$\left\{ \frac{dDR}{dDVV} \right\} = \left[\frac{\partial DR}{\partial FVV} \right] \left\{ \frac{dFVV}{dDVV} \right\} + \left[\frac{\partial DR}{\partial GP} \right] \left\{ \frac{dGP}{dDVV} \right\} + \left\{ \frac{\partial DR}{\partial DVV} \right\} = \{0\} \qquad (14)$$

$$\left\{ \frac{dPOF}{dDVV} \right\} = \left[\frac{\partial POF}{\partial FVV} \right]^T \left\{ \frac{dFVV}{dDVV} \right\} + \left[\frac{\partial POF}{\partial GP} \right]^T \left\{ \frac{dGP}{dDVV} \right\} + \left\{ \frac{\partial POF}{\partial DVV} \right\} \qquad (15)$$

The sensitivity derivatives of the performance objective function in the adjoint method can be calculated by combining Eqs. (14) and (15) as:

$$\left\{ \frac{dPOF}{dDVV} \right\} = \left[\frac{\partial POF}{\partial FVV} \right]^T \left\{ \frac{dFVV}{dDVV} \right\} + \left[\frac{\partial POF}{\partial GP} \right]^T \left\{ \frac{dGP}{dDVV} \right\} + \left\{ \frac{\partial POF}{\partial DVV} \right\}$$
$$+ \psi^T \left(\left[\frac{\partial DR}{\partial FVV} \left\{ \frac{dFVV}{dDVV} \right\} + \left[\frac{\partial DR}{\partial GP} \right] \left\{ \frac{dGP}{dDVV} \right\} + \left\{ \frac{\partial DR}{\partial DVV} \right\} \right] \right) \qquad (16)$$

In Eq. (16), Ψ represents the elements of the adjoint variable vector. Equation (17) can be obtained by reorganizing Eq. (16) [49, 50]:

$$\left\{ \frac{dPOF}{dDVV} \right\} = \left[\frac{\partial POF}{\partial GP} \right]^T \left\{ \frac{dGP}{dDVV} \right\} + \left\{ \frac{\partial POF}{\partial DVV} \right\} + \psi^T \left(\left[\frac{\partial DR}{\partial GP} \right] \left\{ \frac{dGP}{dDVV} \right\} + \left\{ \frac{\partial DR}{\partial DVV} \right\} \right)$$
$$+ \left(\left\{ \frac{\partial POF}{\partial FVV} \right\}^T + \psi^T \left[\frac{\partial DR}{\partial FVV} \right] \right) \left\{ \frac{dFVV}{dDVV} \right\} \qquad (17)$$

The sensitivity derivatives of the performance objective function can be calculated by removing the last term on the right-hand side of Eq. (17):

$$\left\{ \frac{dPOF}{dDVV} \right\} = \left[\frac{\partial POF}{\partial GP} \right]^T \left\{ \frac{dGP}{dDVV} \right\} + \left\{ \frac{\partial POF}{\partial DVV} \right\} + \psi^T \left(\left[\frac{\partial DR}{\partial GP} \right] \left\{ \frac{dGP}{dDVV} \right\} + \left\{ \frac{\partial DR}{\partial DVV} \right\} \right) \qquad (18)$$

Equation (18) can be calculated if and only if the vector Ψ satisfies Eq. (19), and finally, the solution vector Ψ is calculated from Eq. (19):

$$\left[\frac{\partial DR}{\partial FVV} \right]^T \psi + \left\{ \frac{\partial POF}{\partial FVV} \right\} = \{0\}^T \qquad (19)$$

The design criterion (POF) of sensitivity analysis was set for minimizing the total pressure loss in AIP. The analysis was performed by adjoint formulation with the residual accuracy of 0.0001. Figure 11 shows the contour result of shape sensitivity analysis. When the shape sensitivity is plotted on the surface of a body, the locations where this quantity is large indicate where small changes to the surface shape can have a large effect on the observable of interest (AIP total pressure). If the shape sensitivity magnitude is small, then shape changes in this region can be expected to have a small effect on the observable of interest.

It can be deduced from Fig. 11 that the critical regions of geometry are the leading and trailing edges of the VG vanes and other regions have modest effects on the flow improvement. Considering the results of sensitivity analysis and flow streamlines through the VGs region, it was decided to change the profile of the straight VGs, and thus a new S-type profile VG was designed instead of straight ones inside the duct (Fig. 2). It was observed that the design curvature angle of 15 degrees for S-type VGs results in a section profile that is similar to the straight ones (their analysis results are the same as ST1&2 and ST7&8 layouts); thereby, the design curvature angles of S-type VGs were set to be 22.5 and 30 degrees (Table 1).
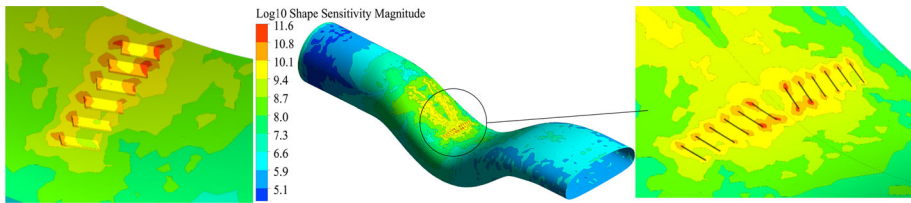
Fig. 11 VGs geometrical sensitivity analysis results of the adjoint solver for minimization of pressure loss at AIP
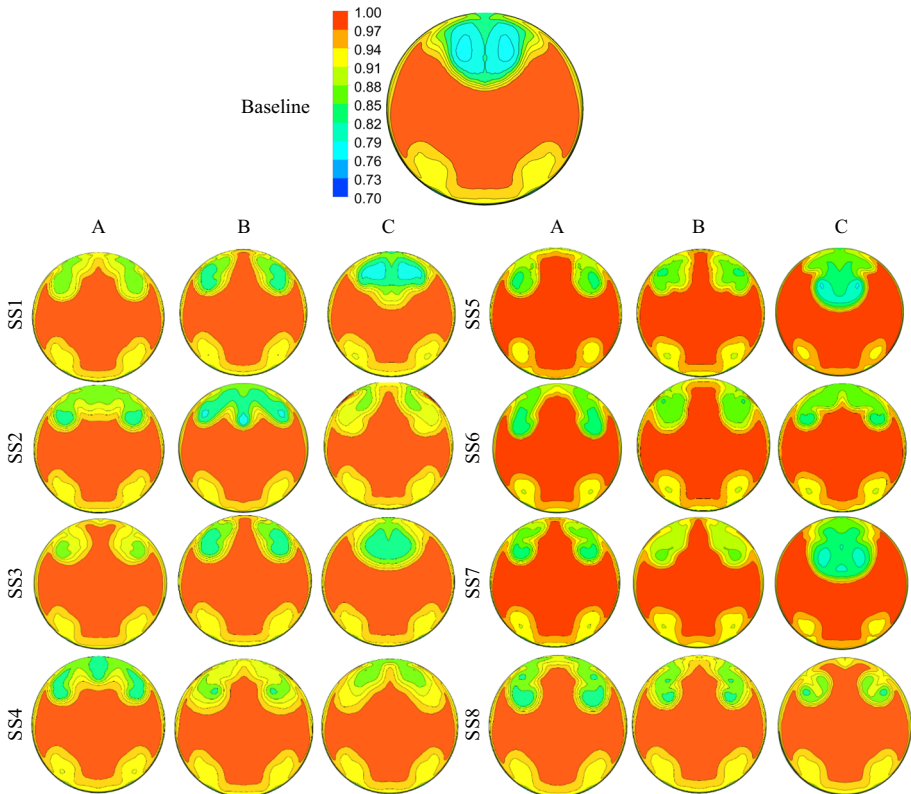

Fig. 12 AIP total pressure contours at S-type VGs design points

5.3 S-type VGs design points

AIP total pressure contours and upper surface CP curve of the S-type VGs DPs are shown in Figs. 12 and 13, respectively. There is a dramatic improvement over the baseline case at the most S-type DPs. VGs could redirect the near wall flow in such a way that the two large vertical structures at the baseline case are substantially attenuated, allowing the flow in the center of the duct to remain attached.

Qualitative comparison of the AIP total pressure contours highlights that the pressure deficit region, which originates from the duct upper surface separation, is significantly diminished in comparison with their analogous straight VGs DPs. The size of the right and left
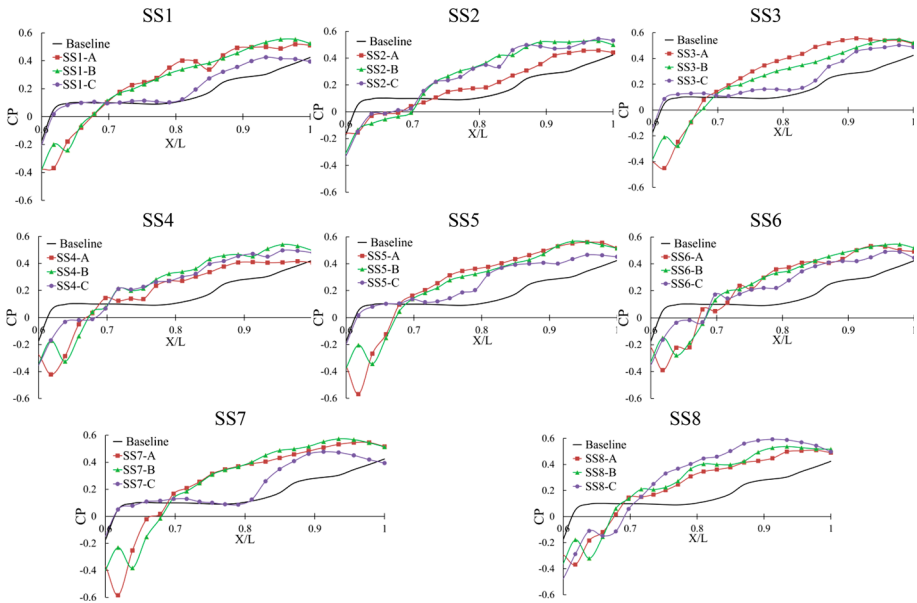
Fig. 13 Duct upper surface CP curves at S-type VGs design points

upper half total pressure deficit regions in AIP is reduced (compared with straight VG ones), and they are completely detached from each other. This signifies the higher effectiveness of S-type VGs.

In the shorter height VGs DPs at C position (SS1, SS3, SS5 and SS7 layouts), the pressure deficit region is more centrally located and accordingly the VGs effectiveness is reduced, which corresponds to the installation of the VG row at downstream of the separation onset point (inside the separation bubble). At these DPs, the pressure plateau region between $0.62 < X/L < 0.8$ signifies the separation of flow at the downstream of VGs (Fig. 13).

By increasing the VG height (at SS2, SS4, SS6 and SS8 layouts), they come out of the separation bubble, and consequently, separation is suppressed at the upper part of the duct.

At the shorter length VGs, increasing VG height reduces the effectiveness of flow control at A and B positions, which is not clearly discernible at $C/L = 0.025$. It can be inferred that increasing VG angle of attack at constant height and length leads to the higher controllability of flow at A and B DPs.

5.4 Flow physics study across the VG vanes

The flow lines across the VG rows are shown for three S-type DPs and their analogous straight ones at Figs. 14, 15 and 16. It can be seen that the curvature and complexity of flow lines at the downstream of VG rows markedly decay at S-type DPs as compared with the straight ones. Furthermore, the local separated flow region immediately downstream of VG row symmetry plane (between left and right sides of VGs) is significantly diminished at S-type VG rows. It can be inferred from the upper surface streamline that the S-type VGs provoke flow to be directed in a way that there is no longer an extensive recirculating region of flow at the downstream of VGs.
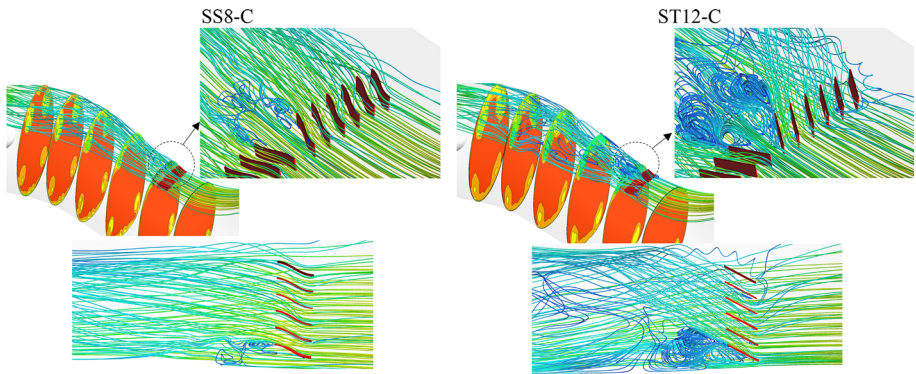
SS8-C

ST12-C

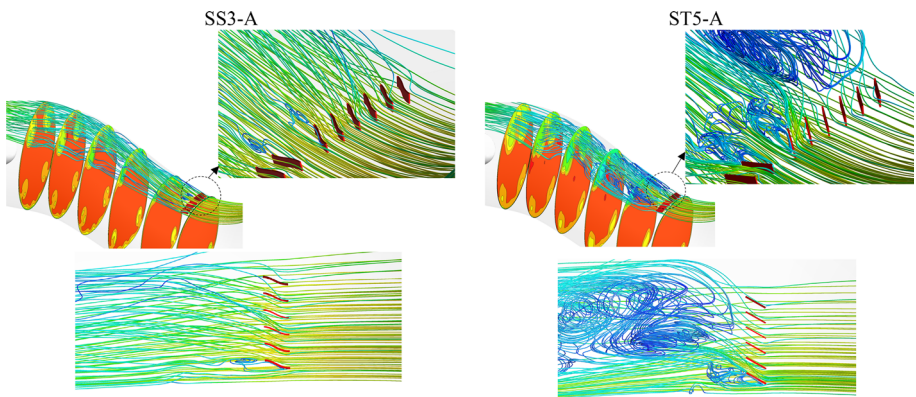**Fig. 14** Comparison of flow lines across VG rows in SS8-C DP and its analogous straight VGs DP (ST12-C)

SS3-A

ST5-A

Fig. 15 Comparison of flow lines across VG rows in SS3-A DP and its analogous straight VGs DP (ST5-A)
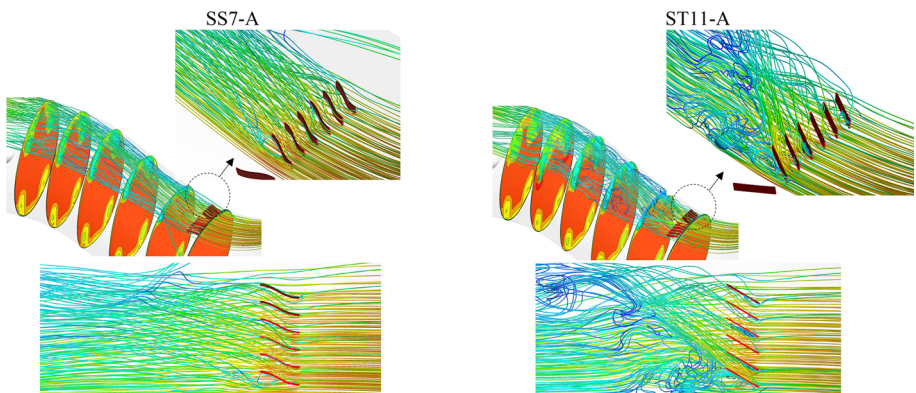
SS7-A

ST11-A

Fig. 16 Comparison of flow lines across VG rows in SS7-A DP and its analogous straight VGs DP (ST11-A)

It can be observed from the flow lines that the flow is extra directed toward the sides of the duct by straight VGs. In S-type ones, due to decrease in angle of attack (incidence angle) and trailing angle of VGs, the curvature and direction of flow lines do not significantly
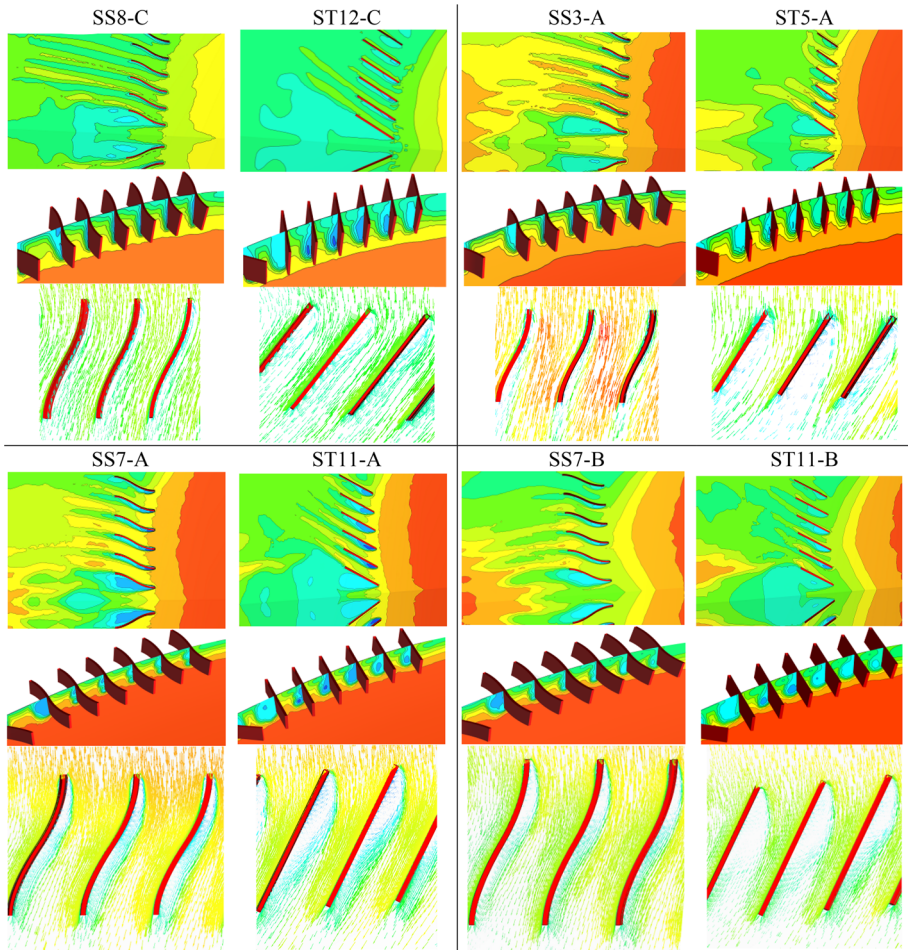
Fig. 17 The total pressure contours and velocity vectors at mid-height VG plane and plane normal to VG rows

change. Accordingly, duct with the S-type VGs incurs the lower total pressure losses across the VGs and facilitates almost uniform flow with small cross-flow velocity components at downstream of the VG row and AIP.

The total pressure contours and velocity vectors are shown in Fig. 17 at the mid-height VG plane and plane normal to the VG rows. The mid-height VG plane vectors show that the flow is broadly separated due to the high VGs angle of attack at straight-type DPs, but in S-type ones, a slight separated flow region is observed at the suction surface of the VGs profile. The total pressure recovery contours also show that the loss regions are significantly decayed in S-type ones and flow has higher pressure recovery at the downstream location of VG rows as compared to their analogous straight VG DPs.

The loss contours at plane normal to VG rows show that, for straight VGs, the pressure losses near the suction surfaces increase from VGs root section and reach the maximum values near the tip region. This trend is not observed in S-type VGs, and there are slight and homogeneous losses near the suction surfaces, which is due to the lower VGs angle of attack.
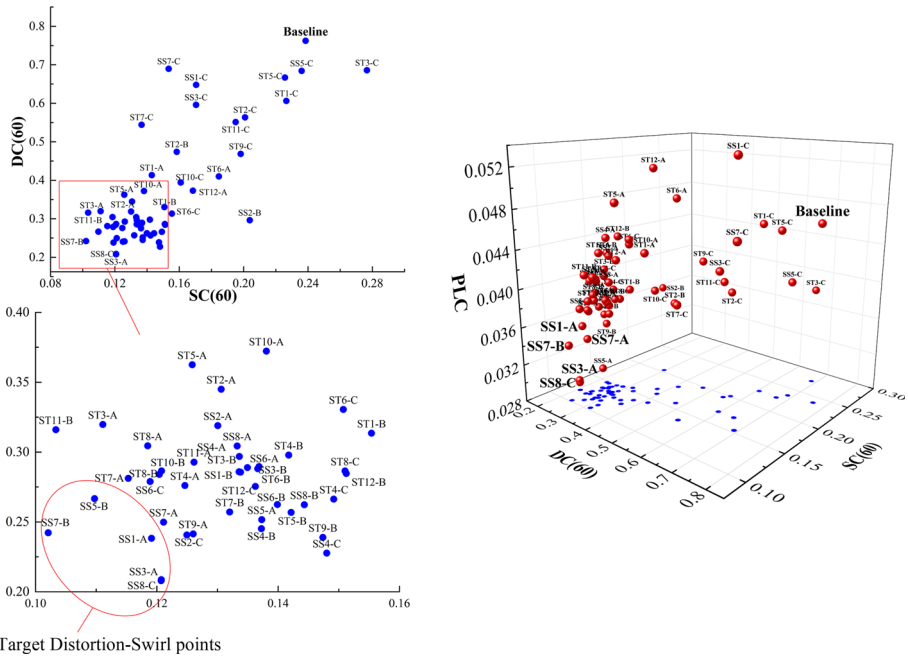
Fig. 18 3D and 2D maps of DPs loss metrics in three aspects of distortion coefficient (DC(60)), swirl coefficient (SC(60)) and total pressure

5.5 AIP flow loss metrics and optimal DPs

In this research, two methods are proposed for achieving optimal DPs. The first way is to use the aspect method. In this method, the flow loss metrics are plotted in three aspects of distortion, swirl and total pressure loss; thereafter, the DPs with the minimum losses are specified in a 3D map graph. In the distortion and swirl aspects, DC(60) versus SC(60) and $\Delta P_C/P$ versus SI metrics are considered together due to their same computational methods (see Sect. 3). The 2D and 3D maps of the DPs are shown in Figs. 18 and 19.

Considering the DC(60) and $\Delta P_C/P$ metrics in comparison with the baseline duct, it can be deduced that the values are different in some instances and even in two ones $\Delta P_C/P$ is increased as compared with the baseline duct (SS5 and SS7 layouts in $X/L = 0.67(C)$ DP (see 2D map in Fig. 19)), while the DC(60) coefficient is decreased (see 2D map in Fig. 18). The maximum reductions in DC(60) (76%) and $\Delta P_C/P$ (78.8%) to the average values of 0.208 and 0.0157 were obtained for the SS3-A and SS4-C DPs, respectively.

Regarding the swirl metrics, the SS7-A&B DPs have the maximum reductions in both swirl descriptors. Most of the excellent DPs have the length of $C/L = 0.025$ that shows the swirl reduction ability of longer length VGs. At the two DPs of ST3-C and ST5-C, SC(60) and SI are increased as compared with the baseline duct. The maximum reductions in SI(43.46%) and SC(60) (57.2%) to the average values of 3.377 and 0.102 were obtained for the SS7-A and SS7-B DPs, respectively.

The 3D maps in Figs. 18 and 19 are shaped by adding the pressure loss coefficient (PLC) as the third aspect to their pertinent 2D (distortion versus swirl) maps. The closest points to the origin of 3D maps are chosen as optimal DPs which comprise the minimum loss points in
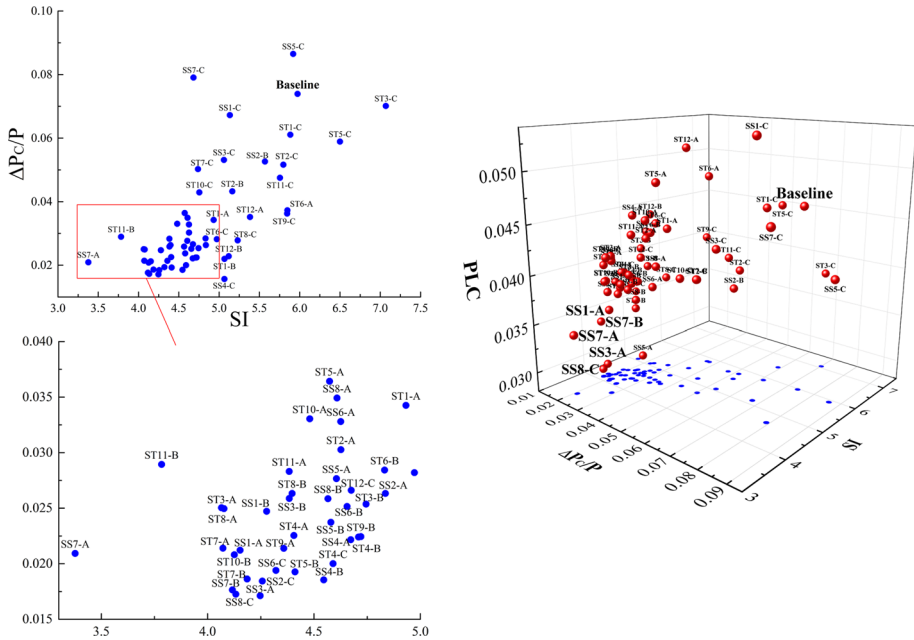
Fig. 19 3D and 2D maps of DPs loss metrics in three fields of circumferential distortion intensity ($\Delta P_C/P$), swirl intensity (SI) and total pressure

three aspects of distortion, swirl and PLC. Fortunately, the optimal DPs are the same for both 3D maps and all of them are the S-type profile DPs (SS8-C, SS3-A, SS7-A&B and SS1-A). It can be concluded that the S-type profile VGs have better performance than the straight ones.

The second way of achieving optimal DPs is the aggregate method. It is possible to aggregate all the flow loss metrics together and compare their percentage reduction with the baseline duct. For this purpose, by considering the equal importance value for all of the loss metrics, their reductions are aggregated for each DP and compared with the baseline case in Fig. 20. It can be deduced that 70% of the ten optimal DPs have S-type profile. As it is observed, the target DPs in the aggregate method are the same as the aspect method.

6 Conclusion

Investigation of design parameters and section profile optimization of the mechanical vane-type vortex generators was performed in a serpentine inlet duct. Secondary flow and separation phenomena arose inside the baseline duct. Due to the weak secondary flow, the attempt was made to suppress the separation at the duct upper surface and mitigate the AIP flow loss metrics by employing the mechanical vane-type VGs in a co-rotating pattern.

The following conclusions can be drawn from the qualitative and quantitative study of the straight- and S-type VGs in the present work:

1. VGs redirected the upper surface separated flow toward the duct side walls and split the AIP upper half total pressure deficit region into two weaker loss regions at the right and left sides of this plane.
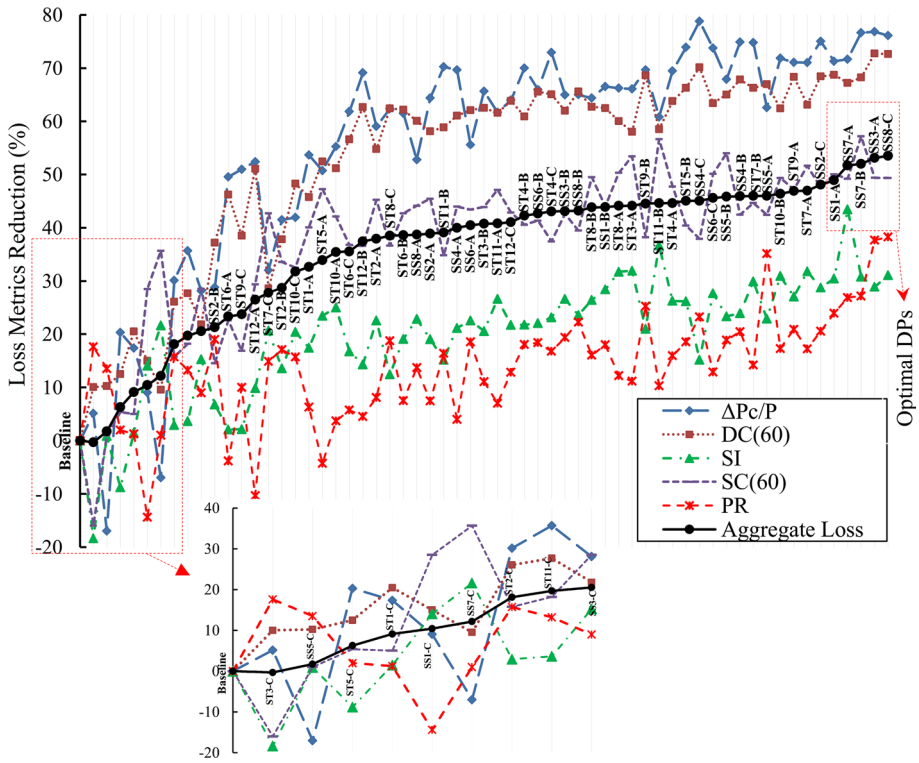
Fig. 20 Percentage reduction of loss metrics and ascending aggregate loss reduction diagram at the duct AIP in all studied DPs

2. Upper surface CP curve indicated that there was no longer a pressure plateau region in the most VGs design points and the curve slope became positive in the separation region.

3. The results of the geometrical sensitivity analysis (of the duct with straight VGs) by adjoint solver revealed that the critical regions of the geometry were the leading and trailing edges of VG vanes.

4. Changing the straight VG profile into S-shape type resulted in a substantial reduction in the curvature of flow streamlines at downstream of the VG row and flow loss metrics at AIP plane, respectively.

5. The mitigation of distortion metrics using S-type VGs was much higher than the swirl metrics.

6. Increasing VGs angle of attack caused a further reduction in the DC(60) and $\Delta P_C/P$ distortion coefficients, and the length and height of the VGs did not significantly affect the distortion metrics.

7. The higher length and shorter height of the VGs caused a further reduction in the SC(60) and SI swirl coefficients, and the VGs angle of attack did not substantially attenuate the swirl metrics.

8. The shorter length and height of the VGs, which was accompanied by the increase in the VGs angle of attack, led to a further reduction in the pressure loss coefficient (PLC).

Table 8 Percentage reduction of the flow loss metrics in optimal DPs

Layout	Design point	Aerodynamic descriptor	Distortion descriptors		Swirl descriptors		Aggregate loss reduction
		Pressure loss	DC(60)	$\Delta P_C/P$	SC(60)	SI	
SS8	C	38.26	72.6	76.1	49.4	31	53.47
SS3	A	37.68	72.7	76.8	49.4	28.9	53.1
SS7	B	27.16	68.2	76.6	57.2	30.8	52
SS7	A	26.86	67.2	71.7	49.22	43.46	51.7
SS1	A	23.91	68.7	71.2	50.05	30.48	48.9

9. Shorter length and height of the VGs at $X/L = 0.67(C)$ DPs located the VG row in the downstream of separation onset and inside the separation bubble. Consequently, flow loss metrics did not improve. The CP curves did not have the local minimums at the longitudinal location of VG row and showed the clear pressure plateau regions between $0.62 < X/L < 0.82$.

10. Over than 60 DPs were studied by using straight- and S-type VGs, and five optimal points were chosen by two methods in three aspects of distortion, swirl and total pressure recovery. All the optimal DPs had an S-type profile, and their percentage reductions of flow loss metrics are tabulated in Table 8.

References

1. M. Monshizadeh et al., Eur. Phys. J. Plus. **2017**, 132 (2017)
2. E. Garnier, AIAA. J. **53**, 2813 (2015)
3. I. Maghsoudi, M. Mahmoodi, M.A.Vazirizanjani, J. Model Eng. **16**, 16 (2018)
4. R.K. Sullerey, S. Mishra, A.M.Pradeep, J. Fluids Eng. Trans. ASME. **124**, 136 (2002)
5. A.R. Paul et al., Aerosp. Sci. Technol. **28**, 332 (2013)
6. A.R. Paul et al., J. Appl. Fluid Mech. **4**, 77 (2011)
7. B.A. Reichert, B.J. Wendt, in *Aerospace Sciences Meeting and Exhibit; 32nd*. (AIAA, Reno, NV; United States, 1994), pp. 14
8. Vakili, et al., in *Shear Flow Control Conference*. (AIAA, Reston, Virigina, 1985)
9. B.H. Anderson, J. Gibb, J. Propul. Power **9**, 442 (1993)
10. B.H. Anderson, J. Gibb, J. Aircr. **35**, 513 (1998)
11. B.G. Allan, L.R. Owens, J.C. Lin, in *44th AIAA Aerospace Sciences Meeting and Exhibit*. (AIAA-2006-1049, Reno, NV, 2006)
12. Y.T. Ng et al., AIAA J. **49**, 1825 (2011)
13. A. Gissen, B.M. Mcmillan, A. Glezer, in *49th AIAA Aerospace Sciences Meeting including the New Horizons Forum and Aerospace Exposition*. (AIAA, Orlando, Florida, 2011)
14. A.N. Gissen, M.L. Mcmillan, A. Glezer, in *41st AIAA Fluid Dynamics Conference and Exhibit*. (AIAA-2011-3096, Honolulu, Hawaii, 2011)
15. M.L. McMillan, et al., NASA CR-2011-217237, 2011
16. J. Yi, C. Kim, B.J. Lee, AIAA J. **50**, 2492 (2012)
17. A. Jirasek, J Aircr. **46**, 8 (2006)
18. G. Tanguy et al., AIAA J. **55**, 1862 (2017)
19. U. Kucuk. Middle East Technical University, 2015
20. P. Aref et al., Aerospace **5**, 23 (2018)
21. Y. Zhang et al., Proc IME J. Power Energ. **229**, 849 (2015)
22. J. Chetboun, G. Allaire, in *8th World Congress on Structural and Multidisciplinary Optimization*. (Lisbon, Portugal, 2009)
23. G. Allaire, in *Congrès Simulation*, edited by SIA. (2015), pp. 5

24. L. Seon seok. Seoul National University Graduate School, 2013
25. S.R. Wellborn, B.A. Reichert, T. Okiishi, AIAA J. Propul. Power. **10**, 668 (1994)
26. A.L. Delot, E. Garnier, D. Pagan, in *47thAIAA/ASME/SAE/ASEE Joint Propulsion Conference & Exhibit*. (AIAA, San Diego,California, 2012), pp. 556
27. J.B. Parham, M. Fitzgerald, E.D.L.R. Blanco, in *49th AIAA Aerospace Sciences Meeting including the New Horizons Forum and Aerospace Exposition*. (Orlando, Florida, 2011)
28. A.R. Paul et al., Sci. World J. **2013**, 8 (2013)
29. S. Tournier, D. Pagan, J.D. Paduano, in *23rd AIAA Applied Aerodynamics Conference*. (AIAA, San Francisco, California, 2005)
30. S. Sun, R.W. Guo, Chin. J. Aeronaut. **19**, 10 (2006)
31. J. Seddon, *Intake Aerodynamic*. Second edn. (Blackwell Science Ltd UK, 1999)
32. SAE, in *SAE-ARP-1420B-Aerospace Recommended Practice*. (Society of Automotive Engineers, 400 Commonwealth Drive, Warrendale, 2011)
33. SAE, in *SAE-AIR-1419A-Aerospace Information Report*. (Society of Automotive Engineers, USA, 2011)
34. P.K. Zachos et al., AIAA J. **54**, 2819 (2016)
35. SAE, in *SAE AIR 5686-Aerospace Information Report*. (Society of Automotive Engineers, Warrendale, PA, USA, 2010)
36. G.D. Prieto et al., AIAA J. **55**, 1878 (2017)
37. D.C. Wilcox, DCW Industries (1998)
38. G.A. Gerolymos et al., J Aircr. **47**, 1368 (2010)
39. Anne-Laure Delot, R.K. Scharnhorst, in *49th AIAA/ASME/SAE/ASEE Joint Propulsion Conference*. (AIAA, San Jose, 2013)
40. S. Kumar, B. Sasanpuri, in *49th AIAA/ASME/SAE/ASEE Joint Propulsion Conference, Joint Propulsion Conferences*. (AIAA, San Jose, 2013)
41. A.P. Pravin Peddiraju, V. Skaperdas, L. Hedges, in *6th BETA CAE International Conference*. (Thessaloniki, Greece, 2015)
42. R.K. Scharnhorst, A.-L. Delot, in *Propulsion and Energy Forum 51st AIAA/SAE/ASEE Joint Propulsion Conference*. (AIAA, Orlando, 2015)
43. K. Saravana, S. Balasubramanyam, in *AIAA SciTech 53rd AIAA Aerospace Sciences Meeting*. (AIAA, Kissimmee, Florida, 2015)
44. S. Kamali, et al., in *AIAA Aviation 33rd AIAA Applied Aerodynamics Conference*. (AIAA, Dallas, TX, 2015)
45. G.A. Gerolymos, I. Vallet, Flow Turbul. Combust. J. **96**, 45 (2016)
46. J. Selvanayagam, et al., in *AIAA Propulsion and Energy Forum 53rd AIAA/SAE/ASEE Joint Propulsion Conference*. (AIAA, Atlanta, 2017)
47. I. Maghsoudi, M.A. Vazirizanjani, M. Mahmoodi, J. Solid Fluid Mech. **7**, 24 (2017)
48. I.B. Celik et al., J. Fluids Eng. Trans. ASME **2018**, 130 (2008)
49. J.B. Lee, C. Kim, Aerosp. Sci. Technol. **11**, 163 (2007)
50. B.J. Lee, C. Kim, O.-H. Rho, in *43rd AIAA Aerospace Sciences Meeting and Exhibit*. (Reno, Nevada, 2005), pp. 14